# Fluid-Structure Interaction Study of the Serpentine Nozzle for Turbofan

P. Sun, L. Zhou[†], Z. X. Wang and J. W. Shi

*Shaanxi Key Laboratory of Internal Aerodynamics in Aero-Engine, School of Power and Energy, Northwestern Polytechnical University, Xi'an, 710072, People's Republic of China*

†*Corresponding Author Email: zhouli@nwpu.edu.cn*

## ABSTRACT

Serpentine nozzle can effectively suppress the infrared radiation signatures of the aero-engine exhaust system. However, it experiences the remarkable fluid-structure interaction (FSI) process at the work condition. In this paper, the deformation behavior of the serpentine nozzle and its flow characteristic were investigated numerically. Then, the influences of the wall thickness and the geometric configuration on the FSI effect were also explored. The results show that, the mechanism of the fluid-structure interaction is formed through the data transfer of the force and the displacement at the FSI interface. Under the FSI effect, there occur the ballon-like swellings at the second S passage, and the linear section bends upward along the Y direction. They induce the special flow features including the flow separation, the shock wave and the plume vector angle. As the value of the wall thickness increases from 3mm to 6mm, the maximum of the deformation displacement of the serpentine nozzle decreases 68.5mm. As compared to the uncoupled state, the variation of the axial thrust decreases from 2.70% to 0.70% at the coupled state. The circular-to-rectangular profile and the S-shaped passage enlarge the deformation behavior of the nozzle structure. The value of the axial thrust of the serpentine nozzle with 5mm wall thickness for the coupled state is lower 1.92% than these for the uncoupled state.

Keywords: Serpentine nozzle; Fluid-structure interaction; Deformation behavior; Flow characteristic; Wall thickness; Circular-to-rectangular profile; S-shaped passage.

## NOMENCLATURE

| | | | |
|---|---|---|---|
| $L/D$ | ratio of axial length to inlet diameter | $W_e/H_e$ | ratio of width to height of nozzle exit |
| $\Delta Y_1/L_1$ | ratio of offset distance to axial length of first S passage | $L_2/L_1$ | axial length ratio of first S passage to second S passage |
| $\Delta Y_2/L_2$ | ratio of offset distance to axial length of second S passage | $\delta_d$ | non-dimensional wall thickness |

## 1. INTRODUCTION

With the rapid advance in the detection technology and the seeking weapon, future military aircraft has to possess the superior mission capability, the combat survivability and the multipurpose function (Sang 2013; Arif *et al.* 2018). The low observable signature has been a necessary technology for the combat aircraft, i.e. stealth performance (Ying *et al.* 2009; Xu *et al.* 2020). The engine exhaust system is the main source of infrared radiation signatures (IRS) in the aircraft (Wang *et al.* 2020; Buchlin 2010; Thillaikumar *et al.* 2020; Song *et al.* 2021). The serpentine nozzle can effectively suppress the infrared radiation signatures of the exhaust system through achieving optical shielding for the high temperature parts inside the aero-engine, and realize the low observable ability of the combat aircraft (Wei *et al.* 2017; Rajkumar *et al.* 2017; Lindermeir and Rutten 2018). Therefore, the serpentine nozzle has been widely applied in advanced stealth aircrafts, such as in the US "B-21" strategic bomber, the "EIKON" UAV of Sweden (Grellmann 1990; Johansson 2006a). The serpentine exhaust nozzle has also been adopted in the US sixth generation adaptive variable cycle engine (Chen *et al.* 2021). However, the geometric configuration of the serpentine nozzle is extremely

complex, including the S-shaped passage with large curvature and the circular-to-rectangular profile, for affording the tremendous tactical mission. Moreover, the composite material and the lightweight structure are extensively adopted in the serpentine nozzle configuration for the sake of low weight (Dalenbring 2006). Correspondingly, the structure property of the serpentine nozzle is more flexible than the conventional circular nozzle. The serpentine nozzle continuously experiences a combined loading environment, including the aerodynamic force, the elevated temperature and the acoustic excitation, when an aircraft travels through the atmosphere during sustained flight with hypersonic speeds. As a result, the serpentine nozzle exhibits the prominent aeroelastic behavior due to the FSI effect, such as the large deformation of the nozzle structure, its limit cycle oscillation and so on. The stability and tactical capability of the engine exhaust system are severely weakened which bring the immeasurable injury to the combat aircraft eventually.

The structural response of the serpentine nozzle in the excessive aerodynamic/thermal/acoustic environment has been concerned by a few researchers. Haney (2006) studied that the influence of the aft deck thickness on the structural response of the serpentine exhaust nozzle washed by the thermal jet. It was shown that increasing the aft deck thickness enables to enhance the structural stiffness nevertheless the adding material will bring the extra load into the surrounding structure. Deaton *et al.* (2010, 2016) conducted a study to characterize the stress-strain characteristics of the serpentine nozzle and its supporting substructure on the basis of the developed thermal-structural analysis framework. They demonstrated that the difference in the thermal expansions between the serpentine nozzle and the substructure causes the large strain at the joint of the two components. On this foundation, the influence of the geometry/aerodynamic parameters on the static thermal elasticity and the modal response of the serpentine exhaust system was further analyzed thoroughly. Vogel (2012) carried a primary research to describe the structural behavior of the serpentine nozzle under the action of the acoustic load. They indicated that, the vibro-acoustic loads are exerted on the wall surface of the exhaust nozzle at a certain excitation frequency which causes the high cycle fatigue life of the nozzle structure. The acoustic pressure evidently reduces while the frequency of the pressure occurring rises through increasing the wall thickness.

For the real work condition of the aero-engine, the elastic structure of the serpentine nozzle continuously interacts with its internal flow field with the elevated temperature and pressure loads which eventually generates the FSI effect. There is the great difference in the aeroelastic behavior of the nozzle structure between the coupling state and the uncoupling state. The FSI effect of the serpentine nozzle has been only investigated by some researchers in the Swedish Defense Agency so far (Smith and Dalenbring 2016; Johansson 2006b). They carried out a numerical simulation in the aeroelastic response of the serpentine nozzle. It was

concluded that the excess pressure load widens the outlet of the linear section in the vertical direction, and the extra annular stiffener can preserve the profile of nozzle exit unchanged. The flow property of the serpentine nozzle in the study is assumed to be inviscid. There is a lack of the deformation mechanism analysis for the serpentine nozzle, and the influence of the structural deformation on the flow characteristics has not been carefully taken into account. The fluid-structure coupling characteristics of the other nozzles with special profiles were investigated by some researchers, the geometric configurations of which are similar to the serpentine nozzle. Nigam and Sricharan (2017) conducted a one-way aero-structural-thermal coupling analysis implementing the ANSYS software in the composite structure of the exhaust system. It indicates that the max von Mises stress of the nozzle structure from the thermal load and the pressure load exceeds the strength of the material, and the contribution of the thermal load to the overall stress far outweighs the effect of pressure load. Urbanczyk and Alonso (2017) performed the optimization of the wall thickness for a supersonic two-dimensional (2D) nozzle design through the high-fidelity one-way aero-structural coupling analysis, and the minimal thickness of the nozzle wall was obtained within the range of the yield strength. It can be observed that the wall thickness is thickened in the areas near the nozzle exit, duct-substructure joints at the inlet and throat. Fenrich and Alonso (2017) carried out a study to describe the one-way aero-structural coupling characteristic of the exhaust composite structure. The distribution of the stress-strain in the exhaust nozzle from the thermal load and the aerodynamic load is clearly clarified, and then the influences of the thermal load and the aerodynamic load on the stress-strain characteristic of the nozzle structure are particularly compared.

The coupling effect between the fluid and structure are not considered in the conventional uncoupling method. There is no data exchange of the pressure load and the deformation displacement. The serpentine nozzle is assumed to be a rigid structure in the flow field calculation, and the influence of the deformation displacement on the distribution of the flow field is ignored. As compared to the uncoupling method, the loosely coupling algorithm enables to accomplish the data exchange between the aerodynamic load and the deformation displacement, and the coupling effect between the flow field and the structural response can be obtained. As an established technique with high stability, it has been widely adopted in the various exhaust systems. Heinrich *et al.* (2011) carried out a CFD/CSD loosely coupling solution for the so called buffeting coupling phenomenon of the rocket nozzle. The CFD computations for this study are performed by the solver TAU, and the ANSYS software is supplied with the CSD analysis. Xiang *et al.* (2013) studied the aeroelastic response of the J-2S rocket nozzle subjected to combined axial thrust and side loads on the basis of the developed two-way loosely coupling platform. Yang *et al.* (2012) connected the FLUENT code with the ABAQUS software through the MPCCI coupling platform where the UDF function

was adopted to analyze gas flow and nozzle deformation. Guo *et al*. (2015) conducted an integrated FSI simulation with the serial loosely coupling algorithm to explore the aeroelastic behavior of the splitter plate during the mode transition in the TBCC exhaust system.

Published literatures have mainly focused on the structural behavior of the serpentine nozzle under the action of the multiphysical loads. Little attention has been paid to the fluid-structure interaction characteristics of the serpentine nozzle, especially to involve the viscous flow, which are only explored preliminarily. The deformation mechanism of the serpentine nozzle and its flow characteristic are currently not clear yet. The S-shaped passage, the circular-to-rectangular profile and the wall thickness are important geometric features of the serpentine nozzle. It is of great significance to investigate the influence of the critical geometric features on the fluid-structure interaction characteristic for the serpentine nozzle geometry with small deformation, high performance and high structural stability. However, it has not been explored. Moreover, the finite element method has been mainly applied in the structural behavior analysis of the serpentine nozzle in the published literatures. There is a certain difference between the numerical results obtained by the finite element analysis and the real physical phenomenon. As compared to the conventional finite element method, the deformation behavior of the serpentine nozzle and its flow field simulated by the coupling calculation method are closer to the real physical phenomenon. The loosely coupling algorithm, as a well-developed technique, has been applied to successfully solve the FSI problem in the other types of the exhaust systems. As a consequence, the aim of this paper is to investigate the fluid-structure interaction characteristics of the serpentine nozzle for turbofan under the condition of the viscous flow in a two-way loosely coupling approach. The outline of this paper is as follows: Firstly, the fluid-structural coupling strategies adopted in this work are introduced, the accuracy of which is tested with the standard Agard445.6 wing case. Secondly, a brief description of the geometric and computational models of the serpentine exhaust nozzle is presented. Then, the study of the fluid-structure interaction characteristics of the serpentine nozzle is performed numerically. The deformation behavior of the nozzle wall and its response mechanism, as well as the flow characteristics inside the nozzle at the deformation stable state are clarified. Finally, the influences of the wall thickness and geometric configurations, including the S-shaped passage and the circular-to-rectangular profile, on the FSI effect of the serpentine nozzle are explored. The "influence of the wall thickness" is described in section 4.2. The "influences of the geometric configurations" is introduced in section 4.3.

## 2. NUMERICAL METHODOLOGY

A CFD solver FLUENT with the finite volume method is adopted to solve the unsteady Reynolds-Averaged Navier-Stokes equations. A CSD solver ABAQUS using the finite element approach is employed to analyze the deformation behavior of the nozzle structure. An unsteady two-way coupling calculation between FLUENT and ABAQUS is implemented by the mesh-based parallel-code coupling interface (MpCCI) platform in a loosely-coupled manner. The MPCCI software is used to control the coupling process and exchange aerodynamic forces and wall displacements across the fluid–structure coupling interfaces.

### 2.1 Fluid Dynamic Solver

FLUENT is employed to precisely capture the high-speed compressible viscous flow field of the serpentine nozzle where the unsteady Reynolds-Averaged Navier-Stokes(RANS)equations are solved by the density-based solver using the finite volume approach. The flow boundary of the nozzle channel sustainedly varies due to the deformation of nozzle wall during the process of the FSI. Then, the Arbitrary Lagrangian-Eulerian(ALE) formulation of the RANS equations is chosen to accomplish the flow simulation for the mesh motion on the coupling interfaces between the fluid and the structure (Guo *et al*. 2013). Correspondingly, it is essential to consider the dynamic mesh while the fluid domain is spatially discretized. The spring-based smoothing and local remeshing methods are combined to reasonably control the distribution of the deformable mesh (Snyder *et al*. 2003; Liu *et al*. 2015). The local remeshing method is specified to sequentially array the regenerated grids near the deformed boundary of the fluid-domain. The total number of regenerated grid nodes increases when the distortion rate and size of the grid elements are larger than the set values. The grid nodes are automatically merged, the total number of which decreases sharply when the distortion rate and size of the grid elements are smaller than the set values. The spring-based smoothing method is employed to automatically adjust the shape of the grid cells which is filled with the altered flow field. This approach regards the grid in the fluid-domain as the "spring nets", and the edges for connecting any node $i$ and node $j$ are idealized as the spring. The spring constant $k_{ij}$ is given by the following:

$$k_{ij} = \frac{1}{\sqrt{\left|\overrightarrow{x_i} - \overrightarrow{x_j}\right|}} \tag{1}$$

Where $\overrightarrow{x_i}$ and $\overrightarrow{x_j}$ represent the coordinate positions of the node $i$ and its adjacent node $j$, respectively. The any cell node acted by elastic force keeps static equilibrium state in the fluid domain when the nodes on the flow boundary move caused by deformed nozzle wall. According to Hook's Law, an iterative formula between the displacements of the node $i$ and its adjacent node $j$ can be expressed as:

$$\Delta\overrightarrow{x_i} = \frac{\sum_j^{N_i} k_{ij}\Delta\overrightarrow{x_j}}{\sum_j^{N_i} k_{ij}} \tag{2}$$

Where $\Delta\vec{x_i}$ and $\Delta\vec{x_j}$ are the displacements of the node $i$ and its adjacent node $j$ . $N_i$ denotes the number of neighbouring nodes connected to node $i$ .

## 2.2 Structural Dynamic Solver

ABAQUS is employed to analyze the deformation behavior of the serpentine nozzle using the finite element approach. This software precisely characterizes the deformation feature of the nozzle structure under the external loads through solving the structural dynamic equation. It is given by (Liu and Qiu 2016):

$$[M]\{\ddot{x}\}+[C]\{\dot{x}\}+[K]\{x\}=\{F(\ddot{x},\dot{x},x)\} \qquad (3)$$

Where $\{x\}$ is the displacement vector. $[M]$ is the mass matrix, $[C]$ is the damping matrix, and $[K]$ is the linear stiffness matrix. $\{F(\ddot{x},\dot{x},x)\}$ is the aerodynamic force vector including the pressure and the viscous stress, which are exerted on the nozzle wall. In order to simplify the structural analysis, the nonlinearity factors of the nozzle structure are not considered in this work. The assumption of Rayleigh damping is adopted to capture the damping behavior of the nozzle structure due to the complexity of the damping mechanism in practice (Chen *et al*. 2016). The equivalent damping matrix can be regarded as the proportional combination of the mass matrix and the stiffness matrix in the finite element method. The expression is defined as:

$$[C]=\alpha[M]+\beta[K] \qquad (4)$$

where $\alpha$ and $\beta$ are the proportional damping coefficients. It can be computed according to the first two orders natural frequencies and the corresponding damping ratios. The expression is given as following:

$$\xi_i = \frac{\alpha}{2\omega_i}+\frac{\beta\omega_i}{2} \qquad (5)$$

where $\omega_i$ is the $i$ th order natural circular frequency. $\xi_i$ denotes the $i$ th order modal damping ratio.

## 2.3 Fluid-Structure Coupling Strategies

The loosely coupling strategies are employed to simulate the fluid-structure interaction characteristic of the serpentine nozzle where a two-way interaction between the fluid and structure conducts the serial staggered algorithm in the time domain (Jaiman *et al*. 2011). The solution of the FSI is implemented by the mesh-based parallel-code coupling interface (MPCCI). As a multi-physics coupling platform, this code enables to accurately control the coupling process and the iterative exchange of data between the FLUENT and ABAQUS codes (Garelli *et al*. 2010; Fraunhofer 2012), as shown in Fig. 1. It is ensured that the time step $\Delta t$ in the flow solver is consistent with that in the structure solver. During each time step $\Delta t$ , the aerodynamic force $F_{\Delta t}$

extracted by FLUENT is transferred to ABAQUS across the coupling interface; then ABAQUS performs the structural analysis under the external load and delivers the obtained wall displacement $U_{\Delta t}$ back to FLUENT; the changed flow field is finally computed by FLUENT according to the constraint of deformed flow boundary. Moreover, it is necessary to exactly capture the initial steady flow field before the unsteady coupling analysis, i.e. at t=0 moment.
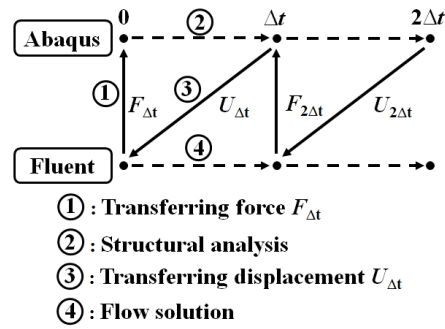


**Fig. 1. The staggered loosely-coupled procedure in the time domain.**

It is difficult to effectively match mesh shapes and node positions between the fluid and structure domains at the both sides of the coupling interface due to the differences in the mesh resolution and the element size. The "association-interpolation" scheme can satisfy the requirement of rapid matching between the fluid and structure meshes (Piperno and Farhat 2001). This algorithm enables to exactly exchange the aerodynamic force $F$ and the displacement $U$ from the source grid to the target grid, as shown in Fig. 2. For the data association, the "neighborhood search" technique is adopted to associate the target cell closest to the source cell so as to build the node-cell relations. For the data interpolation, the aerodynamic force $F$ and the displacement $U$ are separately interpolated at the fluid and solid meshes of the coupling interface based on the shape function mapping approach.
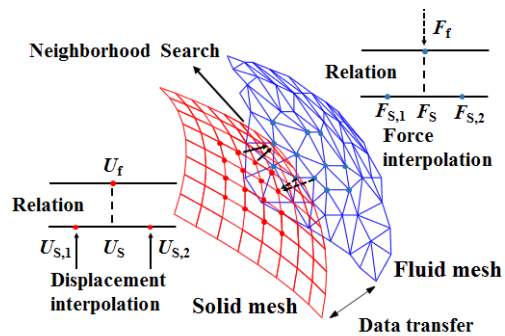


**Fig. 2. Data transfer mechanism in the spatial domain.**

**Table 1 The dimensions and material properties of the Agard 445.6 wing**

| $\rho_s$ /(kg/m³) | $E_s$ /(MPa) | | | $G_s$ /(MPa) | | | $\upsilon_s$ |
|---|---|---|---|---|---|---|---|
| | $E_{11}$ | $E_{22}$ | $E_{33}$ | $G_{12}$ | $G_{13}$ | $G_{23}$ | |
| 381.98 | 3151.1 | 416.2 | 416.2 | 439.2 | 439.2 | 439.2 | 0.31 |

### 2.4 Verification for Coupling Algorithm

Referring to the experimental flutter data of the transonic wing in the NASA Langley Center (Yates 1988), the aeroelasticity simulation of the weakened model of the Agard 445.6 wing is conducted specifically to verify the applicability of the loosely coupling strategies and the MPCCI platform adopted in this paper (Pahlavanloo 2007). The schematic of the geometric profile of the Agard 445.6 wing is presented in Fig. 3, the quarter chord line of which sweeps backward 45 degrees with an aspect ratio of 3.28 and a taper of 0.66. The material properties of the wing structure are isotropic including the density $\rho_s$, the elastic modulus $E_s$, the elastic modulus $G_s$ as well as the Poisson's ratio $\upsilon_s$. The values of them are listed in Table 1. The wing root is clamped, the rest of which is capable of freely vibrating along the Y direction.
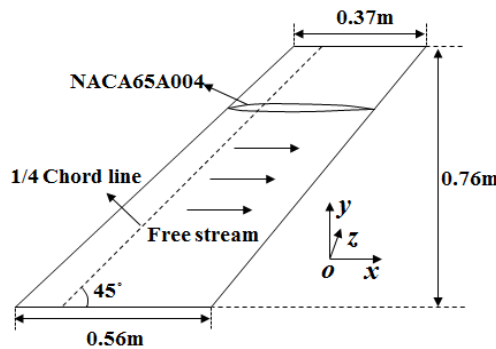


**Fig. 3. Schematic of the geometric profile of the Agard 445.6 wing.**

Inviscid uniform freestream along the X direction flows over the wing. The angle of attack is set to 0, and the density, velocity and pressure of the airflow are symbolled by $\rho_f$, $\mu_f$ and $p_f$. In order to rapidly acquire the aeroelastic behavior of the wing in the time domain, the initial disturbance along the Z direction is imposed on the wing surface. The values of the airflow velocity at the wing flutter threshold are computed based on variation in dynamic pressure under the conditions of different freestream Mach numbers. The Flutter Velocity Index ( $FVI$ ) is defined as the critical dimensionless velocity at the flutter state, and it is expressed as follow:

$$FVI = \frac{\mu_f}{2\pi b f_{t1}\sqrt{\mu}} \qquad (6)$$

Where $\mu_f$ denotes flutter velocity, $b$ is the half root chord, $f_{t1}$ is the angular frequency of the first torsional mode and $\mu$ is the mass ratio between the structural mass and the mass of the equivalent volume of fluid at reference density.

The distributions of the $FVI$ are contrasted among the present result, together with the experimental data (Yates 1988) and other published numerical predictions, as shown in Fig. 4 (Pahlavanloo 2007; Hasse and Selmin 2003). The value of the $FVI$ first drops and then rises with the increase in the Mach number where the "transonic dip" phenomenon is clearly characterized. The value of Mach number is approximate 0.96 while the $FVI$ reaches the minimum. The computational flutter curve is in better agreement with the experimental data as compared to other published literatures, and the predicted value of Mach number corresponding to the minimum of the $FVI$ is also almost equal to the experimental value. Besides, the coupling simulation case under the condition of the 0.85 Mach freestream is chosen to analyze the deformation behavior of the wing model. The distributions of the deformation displacements of the wing model along the span are compared with the numerical results obtained by the other literatures (Cai 2001; Melike *et al.* 2009), as shown in Fig. 5. It can be seen that the distributions of the Y-direction displacements at the leading edge and trailing edge for the wing model agrees well with the results of other literatures. Therefore, the loosely coupling strategies and the MPCCI platform enable to accurately characterize the FSI characteristics of the serpentine nozzle in detail.
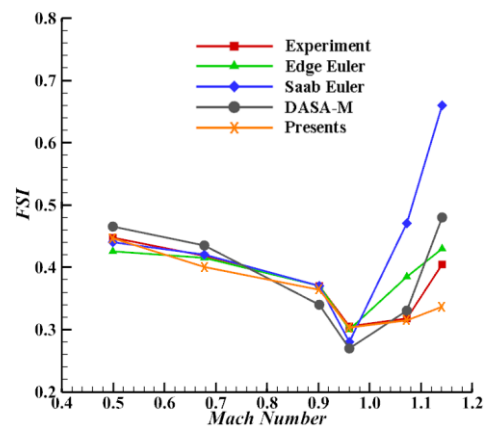


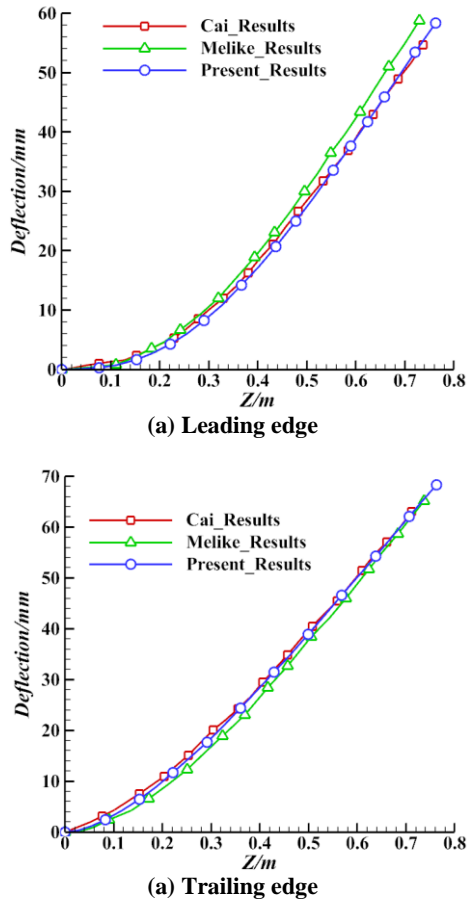**Fig. 4. Distributions of FVI with different airflow Mach number.**

**(a) Leading edge**



**(a) Trailing edge**

**Fig. 5. Distributions of the y-direction deformation displacements of the wing along the span relative to the wing root.**

## 3. GEOMETRIC AND COMPUTATIONAL MODEL

### 3.1 Description of geometric model

The geometric model of the double serpentine exhaust nozzle is built based on a two-spool mixed flow turbofan engine at design point, as shown in Fig. 6. It consists of an axisymmetric entrance section, a double serpentine section and a linear section. The entrance section is simplified into the bypass inlet and the core inlet where the lobed mixer and tail cone are removed. The geometry profiles of the double serpentine section are designed based on the variable section method with diverse parameters coupled (Sun *et al.* 2015). This serpentine section is composed of a series of cross sections normal to the centerline (Jin *et al.* 2015), which monotonically contracts from the circular inlet to the approximate rectangular exit. The non-dimensional values of the critical design parameters are determined by the constraints of the tail cone size at the rear of the aero-

engine and the spatial layout of a certain type of aircraft. They are listed in Table 2. The linear section is a straight channel configuration with the identical area of the rectangular cross section. The quality of the exhaust flow is greatly improved in the linear section.
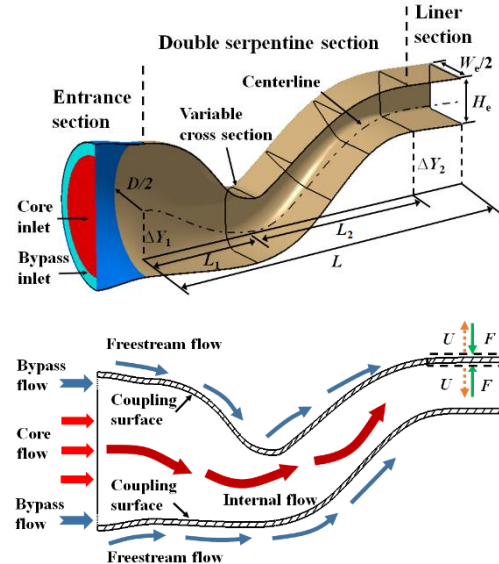


**Fig. 7. Schematic of the fluid-structure interaction model of the double serpentine nozzle.**

The full three dimensional (3D) flow field is spatially discretized using ICEM CFD software. The hybrid mesh with 2.59 million cells is built to fill the fluid computational domain, which is divided into the nozzle domain and the far field domain. The computational grids and boundary conditions are presented in Fig. 8. The nozzle domain is set as the dynamic zone, and it is filled with tetrahedral mesh to adapt the deformable boundary of the flow field. The boundary layer is created near the nozzle wall with triangular prism grids where the y+ values of the first cell are required to satisfy the SST $k$-$\omega$ turbulent model. In order to avoid the creation of the inverted cells due to the mesh deformation, the boundary layer grids are automatically adjusted to stay relatively static with nozzle wall. The far field domain is set as the static zone. It is filled with hexahedral mesh which are non-deformable or not be regenerated. The mesh nodes are merged in the interior between the dynamic zone and the static zone. Second upwind scheme is adopted in the spatial discretization, and Roe-FDS is chosen for the flux type. The coupling time step is set to 2ms in the unsteady simulation.

**Table 2 The values of non-dimensional design parameters**

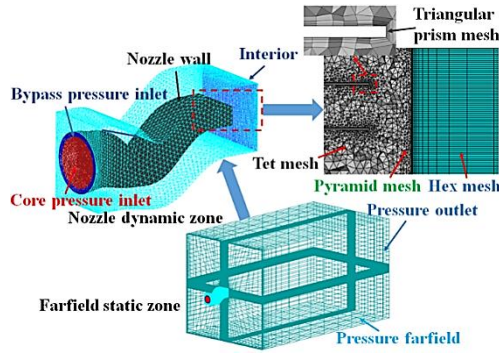| Non-dimensional parameter | $L / D$ | $L_2 / L_1$ | $W_e / H_e$ | $\Delta Y_1 / L_1$ | $\Delta Y_2 / L_2$ |
|---|---|---|---|---|---|
| Value | 2.6 | 1.5 | 3 | -0.3 | 0.36 |

**Fig. 8. Numerical grid and boundary condition of the full 3D fluid domain.**

The computational boundaries of the fluid domain are marched with the design point of a two-spool mixed flow turbofan engine. The influence of the temperature on fluid-structure interaction characteristics is not temporarily considered. The relation between the inlet total pressure of the bypass duct and core duct is calculated by the aero-engine performance simulation model. Pressure inlet conditions with uniform distribution of the total pressure and the total temperature are imposed to the annular inlet of the bypass duct and the circular inlet of the core duct in the nozzle dynamic zone, and the airflow comes in along the axial direction. The values of the total pressure and the total temperature are presented in Table 3. Pressure outlet condition is applied to the exit of the far field domain where the static pressure of 1 atm and the temperature of 300 K are imposed. Other boundaries of the farfield static zone and the nozzle dynamic zone are defined as the pressure farfield condition with $Ma_\infty$=0.05, $P_0$=1atm, and $T_0$=300K. The boundary of the nozzle wall is set to the non-slipped adiabatic wall condition.

**Table 3 Boundary condition settings for the bypass inlet and the core flow inlet**

| Locations | Total pressure(atm) | Total temperature(K) |
|---|---|---|
| Bypass inlet | 1.60 | 300 |
| Core inlet | 1.54 | 300 |

The wall thickness of the solid domain is 3mm. The non-dimensional wall thickness $\delta_d$ of the serpentine nozzle is concluded based on the moment-curvature equation (James and Barry 2016). The $\delta_d$ is expressed by:

$$\delta_d = \frac{nL^2(d+\delta)}{d^2\delta} \tag{7}$$

Where $d$ is the average dimeter of the nozzle; $L$ is the axial length of the nozzle; $\delta$ is the wall thickness of the nozzle structure; n is the constant. The value of $\delta_d$ corresponding to 3mm wall thickness is 1.93. The finite element model of the serpentine nozzle is built using 80316 C3D8I (eight-node linear incompatible modes hexahedral element) elements, as shown in Fig. 9. The high temperature resistant alloy of K491 with isotropic material is chosen for the nozzle

structure, for which the elastic modulus is $E_s$ =20GPa, the material density is $\rho_s$ =7750kg/m$^3$ and the Poisson's ratio is $\mu_s$ =0.28. The nozzle is restricted as a cantilever model, and its inlet face is clamped for restraining the translation and rotation motion of the nozzle structure. Rayleigh damping is assumed with the damping ratio in the structural analysis. The constants of the damping factors $\alpha$ =78.49, $\beta$ =1.2516e$^{-2}$ are respectively ensured to suppress the structural vibration during the fluid-structure coupling process. Gravitational force and heat transfer of the serpentine nozzle are ignored in this work.
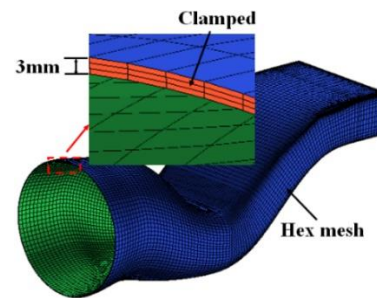


**Fig. 9. Finite element model of the full 3D solid domain.**

### 3.2 Sensitivity Analysis

The grid sensitivity analysis for the fluid domain of the serpentine nozzle is conducted in the present work so as to evaluate the grid-size dependence of the numerical results. Three grids with different resolutions which are separately denoted as the coarse mesh, the medium-fine mesh and the fine mesh, are tested to characterize the FSI characteristic. The aforementioned grids have 1.3 million cells, 2.6million cells and 5.3 million cells in turn. The static pressure on the symmetric wall surface is regarded as the critical variable due to its significance to the FSI simulation, as shown in Fig. 10. It can be seen that the difference in the static pressure among three grids are mainly located
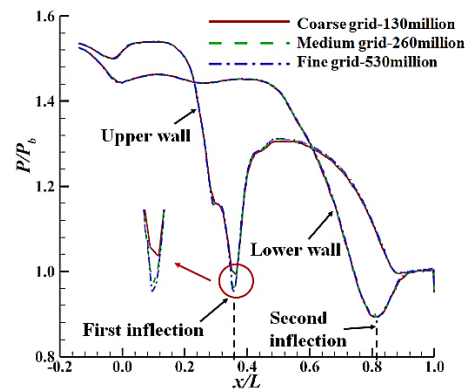


**Fig. 10. Comparisons of the pressure distributions on the symmetric wall surface at the deformation stable state for three grid sizes.**

around the upper wall of the first inflection. The distributions of the static pressure between the medium-fine mesh and the fine mesh are almost undistinguishable while the maximum of the relative error of the static pressure is beyond 2.80% between the coarse mesh and medium-fine mesh. Therefore, the medium-fine mesh with 2.60 million grids is employed to accurately capture the flow characteristics of the serpentine nozzle in the FSI process.

Coupling time step has an essential influence on the FSI simulation with high efficiency and accuracy. Referring to the grid-size dependence and the relative literature (Dalenbring 2006), the sensitivity analysis of the time step size is performed for the FSI computation. Three sets of time step, $\Delta t$=1ms, $\Delta t$=2ms and $\Delta t$=4ms are adopted to characterize the distribution of the static pressure on the symmetric wall surface at the deformation stable state, as shown in Fig. 11. The results indicate that the difference in the static pressure with different time step sizes are mainly located around the upper wall of the first inflection and its downstream region. The maximum of the relative error between the $\Delta t$=2ms and $\Delta t$=4ms reaches 7.85 %. However, it enables to be ignored for for the case between the $\Delta t$=1ms and $\Delta t$=2ms. Consequently, the coupling time step size with $\Delta t$=2ms is adequate for the FSI computation of the serpentine nozzle due to its great advantages in computational cost and solution accuracy.
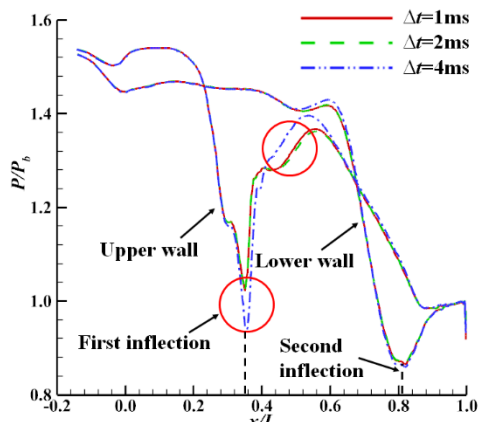


**Fig. 11. Comparisons of the pressure distributions on the symmetric wall surface at the deformation stable state with different time step sizes.**

## 4. RESULTS AND DISCUSSIONS

### 4.1 Fluid-Structure Interaction Characteristic

In order to analyze the fluid-structure interaction characteristic of the serpentine nozzle in detail, Fig. 12 presents the shape profile of the serpentine nozzle and its dimensionless coordinates of the streamwise cross sections. The cross section A is located at the inlet of the serpentine passage. The section B and the section D are situated at the first inflection and the second inflection, respectively. The cross section C

is inside the second S passage. The serpentine passage bends along the Y direction and expands monotonically along the Z direction. The profiles of the upper wall and lower wall are obtained by the nozzle wall intersecting with the XY plane. The profile of the side wall is formed by which the centerline inside the nozzle is projected on the side wall along the Z direction.
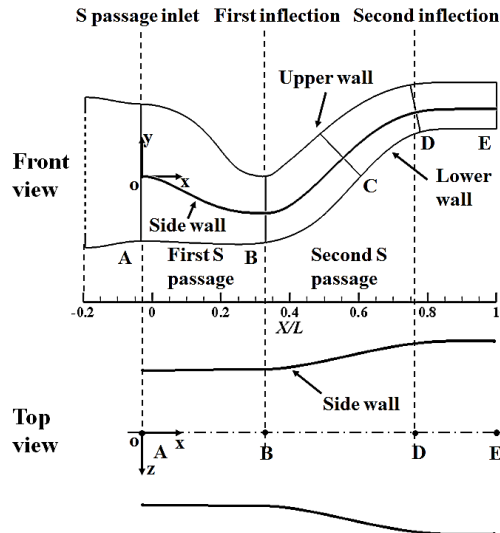


**Fig. 12. Streamwise locations of the cross sections inside the serpentine nozzle.**
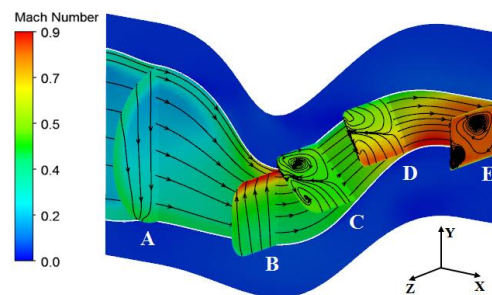


**Fig. 13. Distributions of Ma and streamline inside the serpentine nozzle at the uncoupled state.**

Serpentine nozzle possesses the complex geometric configuration including the serpentine passage with large curvature and the special profile with circular-to-rectangular transition. It leads to the excessively non-uniform flow field inside the nozzle. The internal flow characteristics of the serpentine nozzle at the uncoupled state are presented in Fig. 13. The S-shaped passage induces the airflow deflection along the Y direction inside the serpentine nozzle. It makes that the direction of the streamlines is towards the upper side on the cross section B. The center of the bending curvature is located above the nozzle profile around the first inflection. It leads that the extent of the airflow acceleration around the upper wall is much greater than that around the lower wall at the first inflection. The local region with high velocity is formed at the upper side of the cross

section B due to the violent acceleration. The center of the bending curvature is located under the nozzle profile around the second inflection. The airflow velocity increases obviously around the lower wall when the airflow passes through the second inflection. As a result, the local region with high velocity is formed at the underside of the cross section D. The bending deflection of the airflow inside the S-shaped passage produces a large acceleration loss. The direction of the streamlines is downward at the upper side of the cross section D while it is upward at the underside of the cross section D. The profile of the circular-to-rectangular transition induces the transversal secondary flow along the Z direction, resulting in a large secondary flow loss. The directions of the streamlines around the upper and under sides point from the middle area to the side wall on the cross section D. The profile of the side wall deflects inward downstream of the second inflection along the Z direction, as seen in Fig. 12. It induces a transversal pressure gradient, the direction of which is opposite to that of the secondary flow. The large scope of streamwise vortices are formed on the cross section E under the action of the reverse pressure gradient.

The non-uniform flow field leads to the great complexity in the distribution of the static pressure on the nozzle wall surface, as shown in Fig. 14. There exist local low pressure regions at the upper wall of the first inflection and at the lower wall of the second inflection. These low pressure regions correspond to the local high velocity regions, as shown in Fig. 13. The static pressure on the upper wall gradually drops in the first S passage. It increases rapidly and then decreases continuously in the second S passage. The static pressure on the lower wall remains unchanged in the first S passage. After that it quickly drops in the second S passage. The static pressure on the lower wall rises monotonically after the airstream flows through the second inflection, the value of which is almost consistent with that on the upper wall at the nozzle exit. The static pressure of the side wall gradually decreases in the serpentine passage.

The specific configuration of the serpentine nozzle not only produces the complicated pressure distribution on the nozzle wall, but also enhances the flexibility of the nozzle structure. The non-uniform airflow with the high velocity and pressure transfers the excessive pressure load to the nozzle elastic structure which causes the deformation behavior of the nozzle wall. Conversely, the deformation displacement of the nozzle structure is transferred back to its boundary of the flow field so as to change the characteristics of the internal flow and external jet of the serpentine nozzle. The distribution of the pressure load on the nozzle wall is correspondingly transformed. Consequently, the mechanism of the FSI of the serpentine nozzle is clarified through the iterative exchange between the pressure load and the deformation displacement in the time domain. The aeroelastic behavior of the nozzle structure is close to the stable state when the FSI process reaches the dynamic equilibrium.

The distributions of the deformation displacement of the nozzle structure are presented in Fig. 15. As can
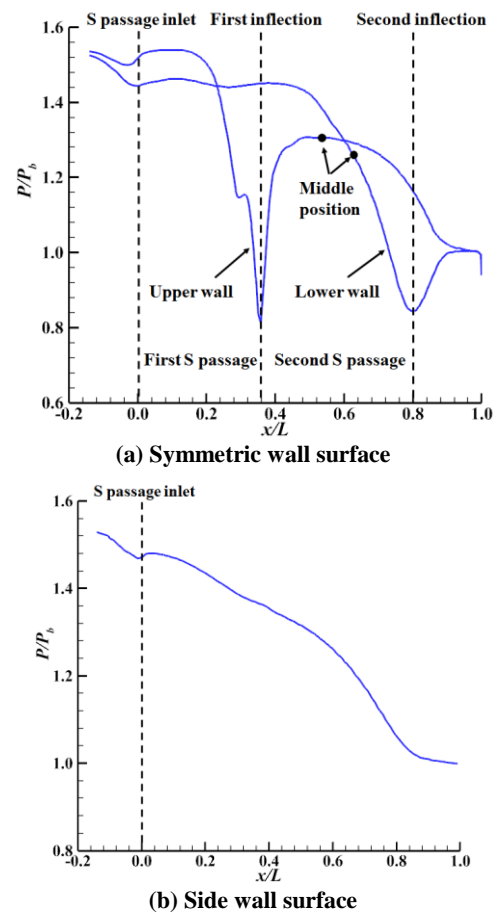


**(a) Symmetric wall surface**



**(b) Side wall surface**

**Fig. 14. Distributions of the static pressure on the nozzle wall surface at the uncoupled state.**

be seen, the deformation behavior of the nozzle structure is rather complex where the deformation displacements on the upper wall and lower wall are evidently larger than these on the side wall. The deformation behavior is principally determined by the pressure distribution on the nozzle wall and its geometric configuration. As shown in Fig. 12 and Fig. 14, the geometric profile and the pressure distribution for the side wall are more gentle than these for the upper wall and lower wall. As a result, the major deformation behavior occurs at the center regions of the second S passage where the local balloon-like swellings are induced by the upper and lower walls bulging outward. The maximum of the deformation displacement is 88.1mm along the Y direction, and it is located at the lower wall. The linear section bends upward since it is subjected to the Y direction pressure gradient at the exit. The local maximum of the deformation displacement at the nozzle exit is 44.2mm, and it is situated at the middle region of the upper wall. Moreover, there exist relatively small structural deformation at the lower wall of the first S passage.

The flow characteristics inside the nozzle are notably altered due to the variation of the flow channel boundary induced by the nozzle structural behavior. The Ma distributions on the symmetric plane and on the cross sections between the coupled state and the
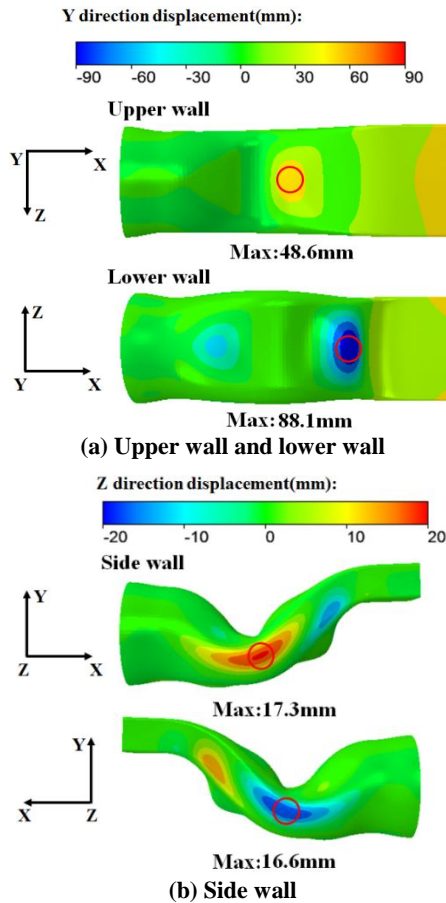
**Fig. 15. Distribution of the deformation displacement of the nozzle structure at the coupled state.**

uncoupled state are separately compared, as shown in Fig. 16. As can be seen in Fig. 16(a), the local

divergent-convergent flow channel is formed at the coupled state owing to the wall bulging outward at the center region of the second S passage. The swelling occurring at the upper wall of the aforementioned region enlarges the bending curvature of the upstream flow channel, and there appear the evident flow separation induced by the large reverse pressure gradient. Correspondingly, Fig. 16(b) presents the large scope separation region at the upper side of the cross section C which extends to the nozzle exit. The swelling occurring at the lower wall of the second S passage enlarges the bending curvature at the second inflection. Then, a distinct shock wave is formed downstream of the second inflection due to the sharp airflow acceleration. It corresponds to the high velocity region with large scope at the lower side of the cross section D in Fig. 16(b). Moreover, the airflow acceleration at the first inflection is effectively weakened by its downstream separation flow. Thus, the flow velocity at the upper side of the cross section B for the coupled state is obviously lower than that for the uncoupled state. The flow separation also appears at the lower wall of the second S passage due to the wall swelling with large deformation displacement. However, the extent of the flow separation for the lower wall is relatively weak as compared to that for the upper wall.

The distributions of the static pressure on the nozzle wall surface between the coupled state and the uncoupled state are contrasted in Fig. 17. As can be seen in Fig. 17(a), the static pressure on the upper

wall of the first inflection with $x$=0.36 for the coupled state is higher than that for the uncoupled state. The reason is that the airflow acceleration at the first inflection is effectively weakened by its downstream separation flow. As compared to the uncoupled state, the static pressure on the lower wall
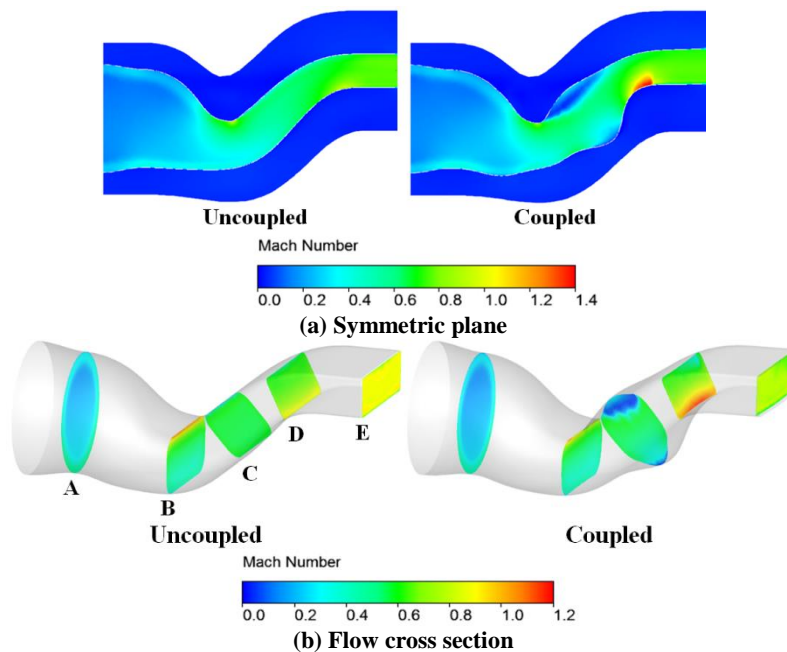


**Fig. 16. Comparisons of Ma distributions inside the serpentine nozzle for two cases.**

of the second inflection with the range from $x$=0.7 to 0.8 obviously decreases at the coupled state due to the sharp airflow acceleration. Corresponding to the position of the shock wave in Fig. 16(a), there exist apparent pressure discontinuity at the second inflection with $x$=0.8 since the airflow is severely over expanded at the coupled state. Moreover, the pressure fluctuation occurs at the lower wall of the second S passage with the range from $x$=0.4 to 0.7 due to the existence of the flow separation induced by the wall swelling. The static pressures at the side wall with the range from $x$=0.3 to 0.5 and $x$=0.6 to 1.0 for the coupled state is notably lower than these for the uncoupled state, as shown in Fig. 17(b). The reduction of the static pressure in the range from $x$=0.3 to 0.5 is caused by the wall bulging outward which increases the divergence angle of the flow channel along the Z direction. The amplitude of the pressure reduction in the range from $x$=0.6 to 1.0 is caused by the sharp airflow acceleration, which is far larger than that in the range from $x$=0.3 to 0.5.



**(a) Upper wall and lower wall**
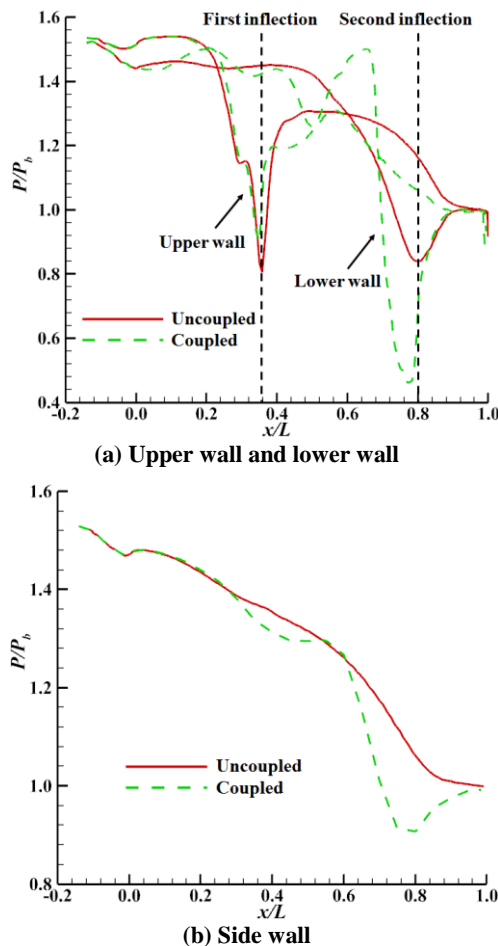


**(b) Side wall**

**Fig. 17. Comparisons of pressure distributions on the wall surface of the serpentine nozzle for two cases.**

The external jet characteristics of the serpentine nozzle are deeply influenced by its structural behavior. Fig. 18 shows the comparison of Ma
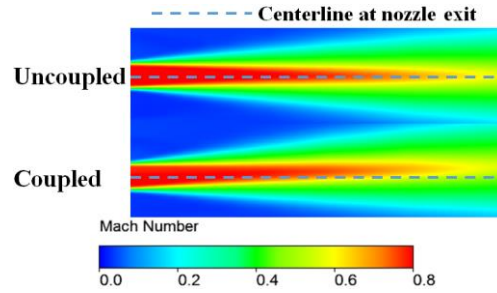


**Fig. 18. Comparisons of Ma contours at the symmetric plane downstream of the serpentine nozzle exit for two cases.**

distributions at the symmetric plane downstream of the nozzle exit between the coupled state and the uncoupled state. It can be seen that the axial length of the plume for above two cases are almost consistent. The reason is that the wetted area of the nozzle exit is invariant for the coupled state compared with that for the uncoupled state. It makes the mixing extent between the bypass flow and the core flow unchanged. This indicates the effect of the FSI on the profile of the nozzle exit can be ignored. However, the linear section bends upward induced by the Y direction pressure gradient at the coupled state, as shown in Fig. 19. It leads to the evident increase in the Y direction velocity of the plume. As a result, the plume deflects upward along the centerline downstream of the nozzle exit.
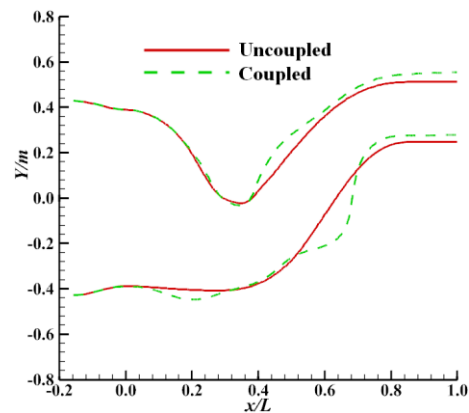


**Fig. 19. Deformation profile on the symmetric wall surface of the serpentine nozzle at the uncoupled state.**

### 4.2 Influence of the Nozzle Wall Thickness

Four groups of the nozzle wall thicknesses in the range of 3mm~6mm are chosen in this paper. The values of the non-dimensional wall thickness $\delta_d$ are 1.93, 1.45, 1.16, 0.97, which corresponds to the 3mm, 4mm, 5mm, 6mm in order. The distributions of the deformation displacement of the serpentine nozzle with selected values of the wall thickness at the coupled state are presented in Fig. 20. The prominent deformation behaviors with different wall thicknesses are represented by the wall swelling occurring at the second S passage and the linear
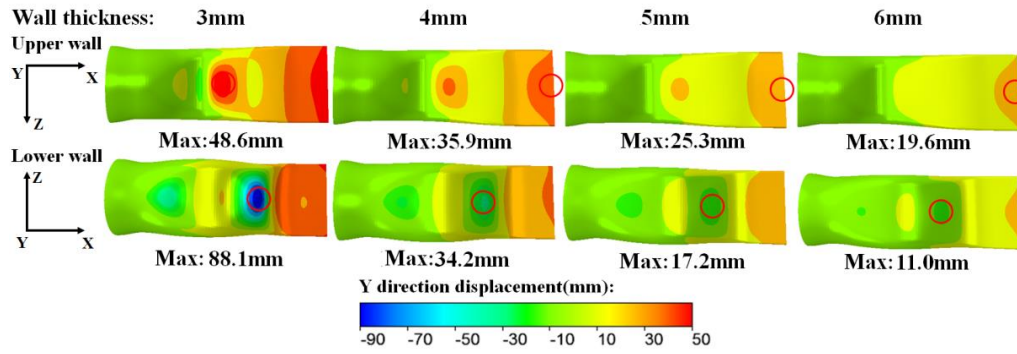
**Fig. 20. Distributions of the deformation displacement of the serpentine nozzle with selected values of the wall thickness.**
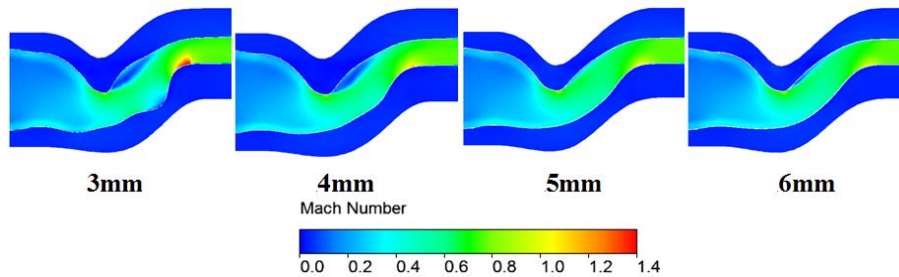


**Fig. 21 Ma distributions on the symmetric plane of the serpentine nozzle with selected values of the wall thickness.**

section bending upward along the Y direction. The values of the deformation displacement at the upper wall and the lower wall gradually decrease as the value of wall thickness rises from 3mm to 6mm. The variation of the max displacement for the upper wall is 29.0mm, which is considerably less than that for the lower wall. The value of the max displacement on the lower wall decreases from 88.1mm to 11.0mm with the increase in the wall thickness range of 3mm~6mm. The max deformation displacement of the nozzle structure is located at the second S passage for the value of the wall thickness with 3mm while it is located at the upper wall of the linear section for the value of the wall thickness with 6mm. The distributions of the deformation displacement on the lower wall with the selected values of the wall thickness are almost consistent, and the max displacements are situated at the center region of the second S passage. There exist a certain difference in the distribution of the deformation displacement of the upper wall with the selected values of the wall thickness. As the value of the wall thickness rises from 3mm to 6mm, the position of the max deformation displacement on the upper wall moves from the second S passage to the linear section.

The Ma distributions on the symmetric plane with selected values of the wall thickness at the coupled state are presented in Fig. 21. As the value of the wall thickness rises, the extent of the local divergent-convergent profile in the second S passage is weakened due to the reduction of the wall swelling. It diminishes the bending curvature of the upper wall downstream of the first inflection where the airflow

separation is effectively suppressed. The airflow separation region vanishes when the wall thickness rises from 3mm to 4mm. Moreover, the bending curvature of the lower wall at the second inflection decreases with the increase in the wall thickness. It weakens the airflow acceleration effect so as to reduces the scope of the supersonic region and the over-expanded situation of the airflow. The shock wave disappears at the second inflection when the value of the wall thickness increases to the 4mm.

The distributions of the static pressure on the symmetric plane with selected values of the wall thickness at the coupled state are presented in Fig. 22. As the value of the wall thickness rises, the wall pressure rises monotonically with the range from $x$=0.7 to 0.8 due to the decrease in the airflow acceleration effect at the lower wall of the second inflection. When the value of the wall thickness rises from 3mm to 4mm, the shock wave disappears at the second inflection where the static pressure on the nozzle wall rises with large amplitude as a result of the reduction of the over-expanded situation of the airflow. Then, the variation amplitude of the static pressure gradually decreases with the value of the wall thickness further increasing. Moreover, the airflow separation caused by the wall swelling is weakened with the increase in the wall thickness. It decreases the fluctuation scope of the static pressure on the lower wall with the range from $x$=0.4 to 0.7. As can also be seen, the static pressure rises in the range of $x$=0.40 to 0.56 while the nozzle wall is monotonically thickened. The reason is that the airflow separation at the upper wall downstream of

the first inflection gradually diminishes However, the suppression effect of the airflow separation on the upstream flow acceleration reduces gradually. Thus, as the value of the wall thickness rises, the static pressure on the upper wall with $x$=0.36 drops monotonically.
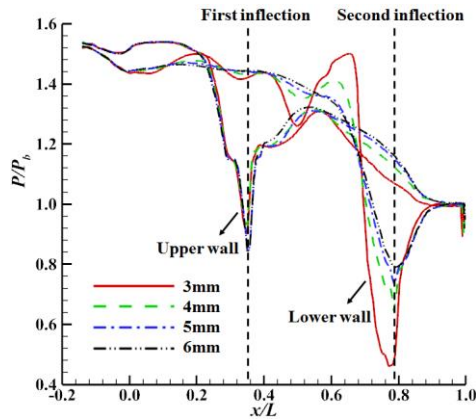


**Fig. 22. Distributions of the static pressure on the symmetric wall surface of the serpentine nozzle with selected values of the wall thickness.**

Figure 23 shows the Ma distributions at the symmetric plane downstream of the nozzle exit with selected values of the wall thickness at the coupled state. As can be seen, the axial lengths of the plume with selected values of the wall thickness are almost consistent. It indicates that the effect of the wall thickness on the deformation behavior of the nozzle exit is negligible, and the wetted areas of the nozzle exit are invariant with different wall thicknesses. However, the ability of resistance to deformation of the nozzle structure strengthens evidently at the coupled state with the increase in the wall thickness, as shown in Fig. 24. The bending extent of the linear section is gradually weakened, the deformation displacement of which drops monotonically along the Y direction. It leads to the gradual reduction in the Y direction velocity of the plume. As a result, the upward deflection angle of the plume monotonically decreases along the centerline downstream of the nozzle exit.

Taking the nozzle performance at the uncoupled state as the benchmark, the variation rate of the aerodynamic performance of the serpentine nozzle with selected values of the wall thickness at the coupled state are listed in Table 4. The wall swelling is rather obvious for the value of the wall thickness with 3mm. It increases the area of the flow channel

remarkably so as to enhance the friction loss of the nozzle wall. As a result, the value of the total pressure recovery coefficient for the coupled state is 2.14% lower than that for the uncoupled state. As the value of the wall thickness rises, the friction loss of the nozzle wall drops due to the reduction of the wall swelling. Consequently, the total pressure recovery coefficient rises monotonically. The value of the total pressure recovery coefficient for the coupled state is only 0.51% lower than that for the uncoupled state when the value of the wall thickness increases to the 6mm. The axial thrust is mostly determined by
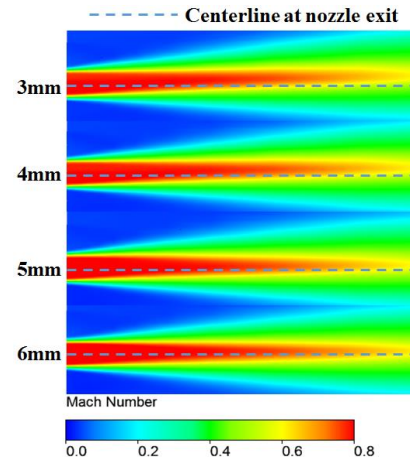


**Fig. 23. Ma distributions on the symmetric plane downstream of the serpentine nozzle exit with selected values of the wall thickness.**
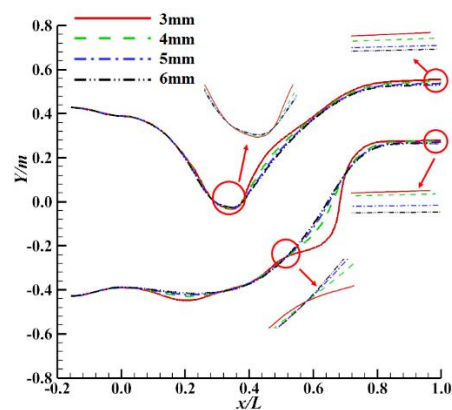


**Fig. 24 The deformation profile on the symmetric wall surface of the serpentine nozzle with selected values of the wall thickness.**

**Table 4 Relative variation rate of aerodynamic performances of the serpentine nozzle with selected values of the wall thickness**

| Wall thickness | Total pressure recovery coefficient | Throat area | Y direction thrust vector angle(°) | Axial thrust |
|---|---|---|---|---|
| 3mm | -2.14% | +1.87% | +1.77 | -2.68% |
| 4mm | -1.22% | +0.71% | +1.25 | -1.67% |
| 5mm | -1.12% | +0.36% | +0.90 | -1.92% |
| 6mm | -0.51% | +0.24% | +0.67 | -0.87% |

the friction loss of the nozzle wall, as well as by the thrust vector angle in Y direction. The friction loss and the thrust vector angle drop monotonically with the increase in the wall thickness so that the axial thrust increases evidently. For the value of wall thickness with 3mm, the value of the axial thrust for the coupled state reduces 2.70% compared with that for the uncoupled state. It only reduces 0.70% for the value of wall thickness with 6mm.

## 4.3 Influence of the Geometric Configurations

The FSI characteristics of the circular nozzle, the two-dimensional(2D) nozzle as well as the serpentine nozzle are comparatively analyzed under the same conditions of the aerodynamic boundary and the structural property, as shown in Fig. 25. The values of the wall thickness of three types of nozzles are 5mm. The geometric configuration of the circular nozzle has almost no structural deformation at the coupled state, which is more stable compared with other two nozzles. The circular nozzle evolves into a 2D nozzle while the circular profile is transformed to the circular-to-rectangular transition. It remarkably strengthens the deformation behavior of the nozzle structure, which is mainly located at the middle region of the upper wall and the lower wall. The maximum of deformation displacement reaches 51.0mm. The circular nozzle evolves into the serpentine nozzle while the profile of the circular-to-rectangular transition is further bended. The position of the major deformation behavior of nozzle structure moves from the middle region to the linear section, and the maximum of the deformation displacement reduces to the 27.6mm. Moreover, there occur the local structural response at the lower wall of the first S passage. Therefore, the circular-to-rectangular profile and the S-shaped passage are the critical geometric features which has a significant influence on the structural behavior of the serpentine nozzle. As compared to the circular nozzle, the circular-to rectangular profile of the serpentine nozzle enlarges its deformation displacement, and the S-shaped passage can effectively inhibit the deformation behavior. However, there appear multiple deformation regions on the nozzle wall surface due to the existence of the S-shaped passage, and the distribution of the wall deformation becomes more complex.

The deformation profiles on the symmetric wall surface of three nozzles with different geometric configurations are shown in Fig. 26. The geometric

profile of the circular nozzle is quite stable, the symmetric wall surface of which is almost invariant at the coupled state. The profile of the circular-to-rectangular transition makes the 2D nozzle become
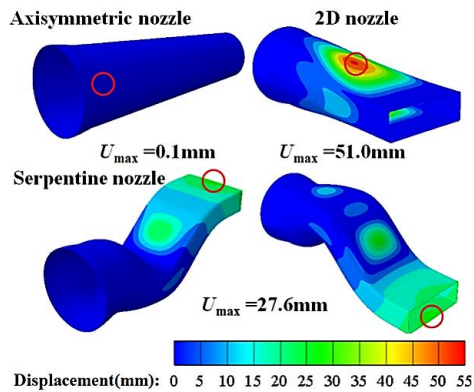


**Fig. 25. Distributions of the deformation displacement of three nozzles with different geometric configurations.**

unstable. The symmetric wall surface with the range from $x/L$=0.2 to 0.8 bulges outward with large deformation displacement at the coupled state. However, the symmetric wall surface sinks inward with the range from $x/L$=0.8 to 1.0. As a result, the outlet area of the 2D nozzle drops while its wetted area rises at the coupled state. The symmetric wall surface of the serpentine nozzle with the range from $x/L$=0.4 to 0.7 bulges outward induced by the circular-to-rectangular profile at the coupled state. The linear section with the range from $x/L$=0.7 to 1.0 bends upward along the Y direction induced by the S-shaped passage. The S-shaped passage also produces the slight deformation behavior at the lower wall with the range from $x/L$=0.1 to 0.3. Consequently, the distribution of the structural deformation of the serpentine nozzle at the coupled state is more complex than that of the other two types of nozzles.

The distributions of the static pressure on the symmetric wall surface of three nozzles with different geometric configurations are presented in Fig. 27. Owing to the structural behavior of the circular nozzle with small deformation, the distribution of the static pressure on the symmetric wall surface of the circular nozzle for the coupled
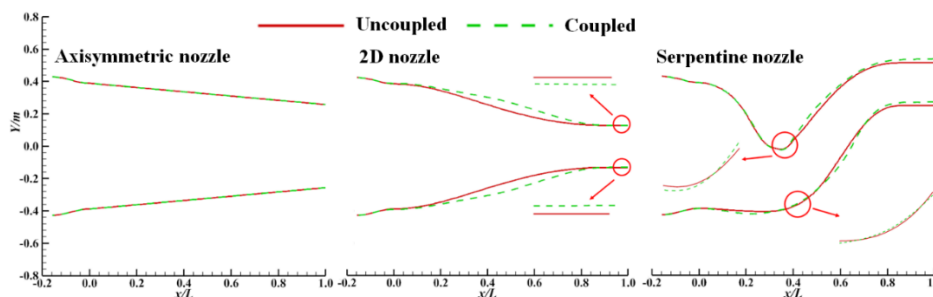


**Fig. 26. Deformation profiles on symmetric wall surface of three nozzles with different geometric configurations.**

state is almost consistent with that for the uncoupled state. The flow channel in the middle region of the 2D nozzle expands sharply under the coupled state due to the existence of the wall swelling. It leads to the acceleration extent of the airflow near the wall weakened in the above region. Thus, the static pressure on the symmetric wall surface with the range from $x/L$=0.2 to 0.8 increases evidently at the coupled state. The S-shaped passage intensifies the complexity in the pressure distribution on the symmetric wall surface of the serpentine nozzle. As the nozzle wall in the range from $x/L$=0.4 to 0.7 bulges outward at the coupled state, the flow separation is formed around the upper wall downstream of the first inflection where the wall pressure reduces with a certain extent. Moreover, the S-shaped passage strengthens the acceleration extent of the airflow at the lower wall of the second inflection. Thus, the static pressure on the symmetric wall surface with the range from $x$=0.7 to 0.8 at the coupled state drops greatly.

Fig. 28 shows the distributions of axial velocity along the centerline downstream of three nozzles exit with different geometric configurations. It can be seen that the velocity distribution on the centerline downstream of the circular nozzle exit for the coupled state is almost consistent with that for the uncoupled state. The rectangular exit of the 2D nozzle sinks inward along the Y direction at the coupled state. It increases the wetted area of the nozzle exit so as to intensify the mixing between the plume and the atmosphere. Thus, the axial velocity on the centerline downstream of the 2D nozzle exit for the couple state is slightly lower than that for the uncoupled state. The plume of the serpentine nozzle at the coupled state deflects along the positive Y direction owing to the linear section bending upward. As a consequence, the axial velocity on the centerline downstream of the serpentine nozzle exit at the coupled state reduces evidently. However, the axial velocity on the centerline around the serpentine nozzle exit rises sharply at the coupled state. The reason is that the core flow through centerline region around the nozzle exit at the uncoupled state is replaced by the bypass flow at the coupled state due to the bending upward profile of the linear section.

Taking the nozzle performance at the uncoupled state as the benchmark, the variation rates of the aerodynamic performance of the circular nozzle, the 2D nozzle and the serpentine nozzle at the coupled state are listed in Table 5. The difference in the aerodynamic performance of the circular nozzle between the coupled state and the uncoupled state can be neglected. The exit section of the 2D nozzle sinks inward in the Y direction under the coupled state so as to decrease the outlet area due to the instability of the rectangular section. The mass flow and the axial thrust for the coupled state are lower 0.7% than these for the uncoupled state. It indicates that the circular-to-rectangular profile has an adverse impact on the aerodynamic performance of the 2D
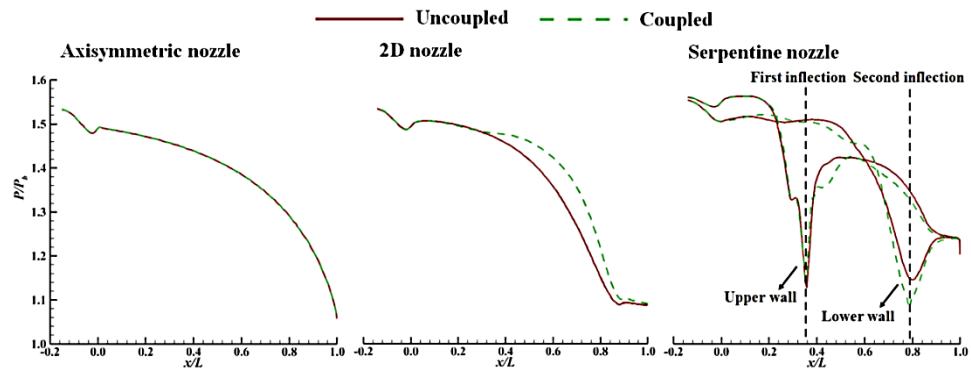


**Fig. 27. Distributions of the static pressure on the symmetric wall surface of three nozzles with different geometric configurations.**
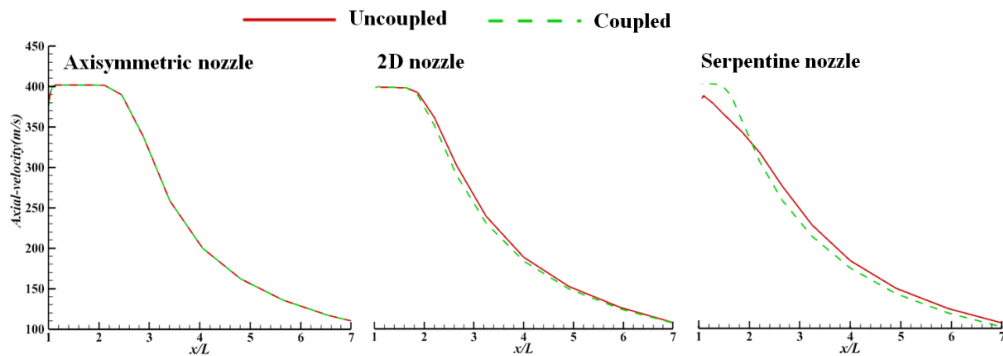


**Fig. 28. Distributions of axial velocity along the centerline downstream of nozzle exit with different geometric configurations.**

**Table 5 Relative variation rate of the aerodynamic performance of three nozzles with different geometric configurations**

| Nozzle types | Total pressure recovery coefficient | Mass flow | Axial thrust |
|---|---|---|---|
| Circle nozzle | 0.00% | 0.00% | 0.00% |
| 2D nozzle | 0.00% | -0.70% | -0.70% |
| Serpentine nozzle | -1.12% | -0.60% | -1.92% |

nozzle by enlarging its deformation behavior. The S-shaped passage intensifies the complexity in the deformation behavior of the serpentine nozzle though it enables to effectively suppress the deformation displacement. This profile increases the friction loss of the nozzle wall, and produces the large thrust vector angle at the coupled state. As a result, the values of the total pressure recovery coefficient, the mass flow as well as the axial thrust of the serpentine nozzle for the coupled state decrease 1.1%, 0.6% and 1.8% separately compared with these for the uncoupled state. The variation rate of the aerodynamic performance for the serpentine nozzle is obviously larger than that for the 2D nozzle.

## 5. CONCLUSION

The fluid-structure interaction (FSI) characteristic of the serpentine nozzle was investigated for turbofan in this paper. The specific conclusions are as follows:

1.  The specific geometric configuration of the serpentine nozzle not only induces the non-uniform flow field on the nozzle wall, but also enhances the flexibility of the nozzle structure. The coupling mechanism is formed through the data transfer of the pressure load produced by the complicated flow field and the deformation displacement of the nozzle elastic structure at the FSI interface.

2.  The major deformation behavior of the serpentine nozzle behaves the local balloon-like swelling which occurs at the middle region of the second S passage. The wall swelling induces the large flow separation and a distinct shock wave inside the nozzle. The linear section bends upward in the Y direction under action of the FSI effect. It causes that the plume downstream of the nozzle exit deflects upward along the Y direction.

3.  As the value of the wall thickness rises from 3mm to 6mm, the wall swelling at the second S passage are weakened, and the bending extent of the linear section decreases gradually. The maximum of the deformation displacement decreases 68.5mm. It causes that the scope of the flow separation is obviously narrowed, and the shock wave disappears inside the nozzle. The deflection angle of the plume also decreases with large amplitude. As compared to the uncoupled state, the reduction of the axial thrust decreases from 2.70% to 0.70% at the coupled state.

4.  The circular-to-rectangular profile enlarges the deformation displacement of the nozzle structure. The mass flow and axial thrust of the 2D nozzle for the coupled state are lower 0.7% than these for the uncoupled state. The S-shaped passage strengthens the complexity in the distribution of the wall deformation of the nozzle structure. The values of the mass flow and the axial thrust of the serpentine nozzle with 5mm wall thickness for the coupled state are separately lower 0.60% and 1.92% than these for the uncoupled state.

## REFERENCES

Arif, I., J. Masud and I. Shah (2018). Computational Analysis of Integrated Engine Exhaust Nozzle on a Supersonic Fighter Aircraft. *Journal of Applied Fluid Mechanics* 11(6), 1511-1520.

Buchlin, J. M. (2010). Convective Heat Transfer and Infrared Thermography (IRTh). *Journal of Applied Fluid Mechanics* 3(1), 55-62.

Cai, J., F. Liu and H. Tsai (2001). Static Aero-Elastic Computation with a Coupled CFD and CSD Method. *39th AIAA Aerospace Sciences Meeting and Exhibit* AIAA 2001-717.

Chen, H. Y., Q. G. Zheng and Y. Gao (2021). Performance Seeking Control of Minimum Infrared Characteristic on Double Bypass Variable Cycle Engine, *Aerospace Science and Technology* 108, 106359.

Chen, Y., J. Zhai and Q. Han (2016). Vibration and Damping Analysis of the Bladed Disk with Damping Hard Coating on Blades. *Aerospace Science and Technology* 58, 248-257.

Deaton, J. D. and R. V. Grandhi (2010). Thermal-Structural Analysis of Engine Exhaust-Washed Structures. *13th AIAA Multidisciplinary Analysis and Optimization Conference* AIAA 2010-9236.

Deaton, J. D., P. A. Berany and D. M. Prattz (2016). On the Trade-off Between Stress and Modal

Responses in the Design of Thermal Structures. *17th AIAA Multidisciplinary Analysis and Optimization Conference* AIAA 2016-4120.

Dalenbring, M. (2006). Analysis of Material and Structure Used Within the FoT25 Project Propulsion Integration. *Swedish Defense Agency* FOI-R-2024-SE.

Fenrich, R. W. and J. J. Alonso (2017). Reliable Multidisciplinary Design of a Supersonic Nozzle Using Multifidelity Surrogates. *18th AIAA/ISSMO Multidisciplinary Analysis and Optimization Conference* AIAA 2017-3826.

Fraunhofer, (2012). Fraunhofer Institute for Algorithms and Scientific Computing SCAI. Germany: *Sankt Augustin*.

Garelli, L., R. R. Paza and M. A. Stortia (2010). Fluid-Structure Interaction Study of the Startup of a Rocket Engine Nozzle. *Computers & Fluids* 39(7), 1208-1218.

Grellmann, H. W. (1990). B-2 Aerodynamic Design. *AIAA Aerospace Engineering Conference and Exhibit* AIAA 1990-1802.

Guo, S., J. L. Xu, J. W. Mo, R. Gu and L. Pang (2015). Fluid Structure Interaction Study of the Splitter Plate in a TBCC Exhaust System During Mode Transition Phase. *Acta Astronautica* 112, 126-139.

Guo, T. Q., Z. L. Lu, D. Tang, T. G. Wang and L. Dong (2013). A CFD/CSD Model for Aeroelastic Calculations of Large-Scale Wind Turbines. *Science China-Technological Sciences* 56(1), 205–211.

Haney, M. A. (2006). *Topology Optimization of Engine Exhaust-Washed Structures*. Dayton: Wright State University.

Hasse, W. and V. Selmin (2003). Progress in Computational Flow-Structure Interaction. Germany: *Library of Congress Cataloging-in-Publication-Data*.

Henrich, L. and J. B. Calvo (2011). A Fluid Structure Coupling of the Ariane-5 During Start Phase by DES. *CEAS Space Journal* 1, 33-44.

Jaiman, R., P. Geubelle and E. Loth (2011). Transient Fluid–Structure Interaction with Non-matching Spatial and Temporal Discretizations. *Computers & Fluids* 50(1), 120–135.

James, M. G. and J. G. Barry (2016). *Mechanics of Materials*. US: Stanford University.

Jin, D. H., X. W. Liu and W. G. Zhao (2015). Optimization of Endwall Contouring in Axial Compressor S-Shaped Ducts. *Chinese Journal of Aeronautics* 28(4), 1076–1086.

Johansson, M. (2006a). Propulsion Integration in an UAV. *24th AIAA Applied Aerodynamics Conference* AIAA 2006-2834.

Johansson, M. (2006b). Fot25 2003-2005 Propulsion Integration Final Report. *Swedish Defense Agency* FOI-R-2017-SE.

Lindermeir, E. and M. Rutten (2018). IR-Signature of the MULDICON Configuration Determined by the IR-Signature Model MIRA. *36th Applied Aerodynamics Conference* AIAA 2018-3166.

Liu, C. F. and J. Qiu (2016). *Analysis Methodology of Fluid Structure Coupling of Aeroelasticity*. Beijing: Beijing University of Aeronautics and Astronautics Press.

Liu, J., H. C. Yuan, and R. W. Guo (2015). Unsteady Flow Characteristic Analysis of Turbine Based Combined Cycle (TBCC) Inlet Mode Transition. *Propulsion and Power Research* 4(3), 141–149.

Melike, N., L. Oncu and A. Aysan (2009). Multidisciplinary Code Coupling for Analysis and Optimization of Aeroelastic Systems. *Journal of Aircraft* 46(6), 1938-1945.

Nigam, N. and A. Sricharan (2017). Design Optimization of Advanced Exhaust Systems. *18th AIAA/ISSMO Multidisciplinary Analysis and Optimization Conference* AIAA 2017-3331.

Pahlavanloo, P. (2007). Dynamic Aeroelastic Simulation of the Agard 445.6 Wing Using Edge. *Swedish Defense Agency* FOI-R-2259-SE.

Piperno, S. and C. Farhat (2001). Partitioned Procedures for the Transient Solution of Coupled Aeroelastic Problems—Part II: Energy Transfer Analysis and Three-Dimensional Applications. *Computer Methods Applied Mechanics and Engineering* 190(24-25), 3147-3170.

Rajkumar, P., S. T. Chandra and A Kushari (2017). Flow Characterization for a Shallow Single Serpentine Nozzle with Aft Deck. *Journal of Propulsion and Power* 33(5), 1130–1139.

Sang, J. H. (2013). *Low Observable Technologies of Aircraft*. Beijing: Aviation Industry Press.

Song, F., L. Zhou, J. W. Shi and Z. X. Wang (2021). Investigation on Flow Characteristics and Parameters Optimization of a New Concept of TC Nozzle. *Journal of Applied Fluid Mechanics* 14(3), 819-832.

Smith, J. and M. Dalenbring (2016). Aeroelastic Simulation of S-duct Dynamics Using Structure-Coupled CFD. *25th Congress of the International Council of the Aeronautical Sciences*.

Snyder, D., E. Koutsavdis and J. Anttonen (2003). Transonic Store Separation Using Unstructured CFD with Dynamic Meshing. *33rd AIAA Fluid Dynamics Conference and Exhibit* AIAA 2003-3919.

Sun, X. L., Z. X. Wang and L. Zhou (2015). The Design Method of Serpentine Stealth Nozzle Based on Coupled Parameters. *Journal of Engineering Thermophysics* 36(11), 2371-2375.

Thillaikumar, T., P. Bhale and M. Kaushik (2020). Experimental Investigations on the Strut Controlled Thrust Vectoring of a Supersonic Nozzle. *Journal of Applied Fluid Mechanics* 13(4), 1223-1232.

Urbanczyk, P. and J. J. Alonso (2017). Coupled Multiphysics Analysis for Design of Advanced Exhaust Systems. *58th AIAA/ASCE/AHS/ASC Structures, Structural Dynamics, and Materials Conference*. AIAA 2017-0799.

Vogel, R. N. and R. V. Grandhi (2012). Structural Acoustic Analysis and Design of Aircraft Components. *12th AIAA ATIO Conference and 14th AIAA/ISSM Conference*. AIAA 2012-5557.

Wang, W. J., L. Zhou, Z. X. Wang and J. W. Shi (2020). Influence of Geometric Parameters on Overall Performance of High Bypass Ratio Turbofan Nacelle and Exhaust System. *Journal of Applied Fluid Mechanics* 13(6), 1959-1973.

Wei, D. H., S. S. Tang and H. Jin (2017). Analysis and Discussion on Stealth Technology of Aero-Engine. *Aeronautical Science & Technology* 10, 1–7.

Xiang, Z., S Bayyuk and Z. S. Jun (2013). Aeroelastic Response of Rocket Nozzles to Asymmetric Thrust Loading. *Computers & Fluids* 76, 128-148.

Xu, D. G., J. Q. Ai, W. T. Lei and L. B. Wang (2020). Analysis on Stealth Requirement of Next-Generation Bomber in the Future. *Advances in Aeronautical Science and Engineering* 9(4), 451–457.

Yang, Y. C., P. P. Wu and S. W. Gao (2012). Rapid Pressurization Side Load Fluid-Structure Coupled Analysis in SRM Nozzle. *Journal of Solid Rocket Technology* 35(4), 463-473.

Yates, E. C. (1988). Agard Standard Aeroelastic Configurations for Dynamic Response Candidate Configuration I-Wing 445. *NASA Technical Memorandum*. 100492.

Ying, L., W. Zhe, H. Peilin and Z. Liu (2009). A New Method for Analyzing Integrated Stealth Ability of Penetration Aircraft. *Chinese Journal of Aeronautics* 23, 187–193.